Larhyss Journal, ISSN 1112-3680, n°56, Dec 2023, pp. 139-178

CURVED WALL TRIANGULAR FLUME (CWTF) DESIGN, THEORY, AND EXPERIMENT

ACHOUR B. [1*]***, DE LAPRAY G.*** [2]

[1] Research Laboratory in Subterranean and Surface Hydraulics (LARHYSS), University of Biskra, Algeria,
[2] Former professor emeritus of the National Polytechnic School of Algiers, Hydraulic Department, Algeria

(*) bachir.achour@larhyss.net

Research Article – Available at http://larhyss.net/ojs/index.php/larhyss/index
Received April 15, 2023, Received in revised form December 2, 2023, Accepted December 4, 2023

ABSTRACT

The flumes reported in the specialized literature are mostly designed in a rectangular shape, such as the Parshall or the Venturi, which has several drawbacks, in particular low accuracy for low flow depths. The section that offers the best accuracy for both low and high flow rates is the triangular section on which the measuring device under consideration is based.

The dimensions of the device are well defined based on rigorous geometrical considerations, with the exception of the length of the throat, which has been derived from an in-depth graphical optimization study. To facilitate the calculations, all the dimensions of the device are related to the top width B_o of the approach channel, which is a known parameter for a given installation.

The discharge coefficient relationship C_d is derived using two distinct rational methods: one is based on the energy equation, and the other is based on the properties of the kinetic factor.

The experimental tests were carried out on a specially designed installation involving eight devices that allowed the collection of 1485 experimental values of C_d. The predicted discharge coefficients had excellent agreement with the observations since a maximum deviation of only 0.07% was observed.

Keywords: Flume, Weir, Triangular profile, Discharge, Discharge coefficient, CWTF.

INTRODUCTION

The specialized man-made canals used for flow measurement in open channels are well known as flumes. Typical flumes, such as the Parshall and Venturi flumes (Parshall, 1936; Henderson, 1966; Bos, 1976; Bos, 1989), are generally made up of a solidary set of three successive static parts from upstream to downstream: a converging section, a throat, and a diverging section, also known as discharge. This configuration is not fortuitous because each of the parts, as it is designed, plays a primordial role in the behavior of the flow and in the control of the flow rate.

The role of the converging section is to restrict the flow that undergoes a significant acceleration, passing from a subcritical state upstream to a supercritical state downstream.

It is worth noting that flumes can also restrict flow and accelerate it, resulting in a localized change in the elevation of the bottom. Sometimes, certain flumes are designed with both a contraction of the sidewalls and a change in elevation.

This supercritical state of the flow thus even remains inside the throat, necessarily passing through a critical state occurring most often in the inlet section of the throat. Either way, this section, often called the "control section", is located in a specific region of the throat that controls flow to produce the stage-to-flow rate relationship. It is thus well understood that the creation of a control section is the prerequisite condition for an appropriate functioning of the device, i.e., a needful particular state flow that allows the canal to play its role as a flowmeter.

As it is not known where exactly the control section is located inside the throat, it is advisable to provide the throat with a sufficient length to allow parallel flow stream lines in this section.

The diverging section has two main roles. The first consists of ensuring the transition between the outlet of the throat and the downstream channel walls where the device is inserted. The second role, which is the most important role, consists of accommodating a hydraulic jump. This is generally caused by local discontinuities in the throat, such as a drop or an elevation of its bottom. These local discontinuities not only contribute to the formation of the hydraulic jump but also maintain it over a wide range of flow rates. The formation of the hydraulic jump, located between the throat and the converging section, has the role of raising the downstream water level so that the device operates with minimum head losses. This configuration is very sought after in practice when the device is used in areas with a slight slope (Achour, 1984). Head losses are experimentally estimated to be between approximately 6% and 7% depending on the type of device, which is equivalent to a semimodularity limit between 93% and 94%.

The other important role of the hydraulic jump, when it forms between the throat and the converging section, is that its upstream water level is sufficient to cause the effective priming of siphons placed along the walls of the channel. These are previously sized to provide the flow rate required for irrigation needs (Achour, 1984).

The aforementioned stage-to-flow rate relationship, that is, the relationship between the upstream water level and the flow rate, is known as the stage-discharge relationship. This means that the flow rate Q can be determined in the upstream part of the device by operating a single depth reading at a specific point of measurement whose location depends on the type of flume. For the Montana flume, the depth measurement location is inside the device at a distance that depends on the flume size (United States Department of the Interior). In contrast, for the original Parshall flume, the flow depth measurement section is located two-thirds the length of the converging section, counted from the throat, or, alternatively, one-third the length of the converging section counted from the inlet section (Achour, 1984; Carlier, 1998).

When the control section is located inside the throat, the criticality condition properties (Henderson, 1966; Bos, 1976), along with some simplifying assumptions, are exploited to analytically derive the stage-discharge relationship. This is the case for all devices called "long-throated flumes", such as Palmer-Bowlus or RBC (ASTM D5390-93, Clemens et al., 1984); however, contrary to what some literature claims, this is also valid for some of the devices referred to as "short-throated flumes", such as the Parshall flume (Achour et al., 2003).

For the aforementioned devices, the theoretical stage-discharge relationship is written as$Q = C\ W\ h_1^n$, where C is a constant, W is the width of the throat, h_1 is the measured upstream flow depth, and the exponent n is equal to 3/2, which is in full conformity with rectangular cross-sections. However, the previous relationship is often corrected by the effects of a correction factor that takes into account the simplifying hypotheses. Nevertheless, the practical stage-discharge relationship recommended by Parshall is the following improved one, written in engineering units as $Q = 372\ \times W\ \times 3.28^x \times h_1^x$, where the exponent x depends solely on the throat width W and whose values are tabulated; it varies in the range [1.506; 1.609] when W varies in the following corresponding range [0.20 m; 2.60 m] (Carlier, 1998). The above stage-discharge relationship gives the flow rate Q at ±2% to ±5%, sometimes even ±7%. It is worth noting that this accuracy is similar to that induced by most weirs (Vatankhah and Khamisabadi, 2019).

The Parshall is not the only device belonging to the class of "short-throated flumes". Its citation herein is unavoidable because it is the most popular flume. However, there are also other short-throated flumes used in hydraulic engineering practice. One of the most coveted is the H-flume, which is not a channel in the proper sense of the term but rather a modified weir, despite being classified as a short-throated flume (Gwinn and Parsons, 1976). The letter *H*, associated with the name of the device, actually corresponds to the eighth letter of the alphabet. The name H-flume is not related to the shape of the device as one might suppose, but it is only the eighth device investigated among a long series of devices. The designers of this device attempted to combine the acuteness of a narrow-angle triangular weir with the self-cleaning properties of a flat bottomed flume. The *H*-flume is devoid of diverging sections, making the device take up less space. Moreover, it can measure a much wider range of flow rates than any other type of channel of the same

class. No known study has attempted to infer the stage-discharge relation of the H-flume analytically.

The class of short-throated flumes also includes the USGS Portable Parshall flume, which is a modification of the original Parshall. This modification consisted of removing the diverging section to make the device lighter and easier to handle (Johnson, 1963; Kilpatrick and Schneider, 1983). The device is presized at 3 inches, which corresponds to the width of the throat. It is recommended that the device be used under conditions of free fall flow at the exit of the throat. The device has not been the subject of any theoretical investigation. The stage-discharge relationship has been determined experimentally and is written as $Q = 1.142h_1^{1.58}$, where Q is in CFS units and h_1 is in feet. The main observation is that the exponent 1.58 is not in conformity with rectangular sections and does not correspond to any known and established principle of fluid mechanics. The exponent should be, without any contest, equal to 3/2. The proposed formula is certainly practical; however, it does not conform to the theory of flume rectangular sections.

Another interesting short-throated flume from a shape perspective is the trapezoidal flume characterized by a V-shaped cross-section, which extends for some distance, and a flat bottom (Robinson and Chamberlain, 1960; Robinson, 1966). A short diverging trapezoidal section ensures the transition between the trapezoidal channel, which is the inlet of the device, and the triangular cross-section channel, which is finally followed by a diverging trapezoidal cross-section canal corresponding to the discharge.

In their major study, Ackers and Harrison (1963) gave a full report on development carried out on trapezoidal flumes at the hydraulics research station of Wallingford. They highlighted foremost that observation meriting particular attention is that the device calibration curve can be derived, with satisfactory accuracy, from the boundary layer concept involving a drag coefficient. Friction losses within the flume, based on the Darcy-Weisbach friction factor, were determined as a function of the Reynolds number. Additionally, design methods were recommended to determine the flume dimensions for a particular situation.

One of the short-throated flumes that truly caught on during the early 1970s and continues to generate interest today, especially in the United States, is the Cutthroat Flume (Skogerboe et al., 1972). Its name comes from the fact that it is a throat-devoid flume; hence, it is composed solely of a converging and a diverging section. There are two forms of the device, namely, the rectangular cutthroat flume and the trapezoidal cutthroat flume (Samani, 2017). The flume has the ability to overcome the limitations of Parshall when it is used in flat gradient areas exposed to significant head losses. One cannot understate the fact that the rectangular cutthroat flume requires no laboratory evaluation when designed with a new size. Specialized literature indicates that the Cutthroat Flume was designed to provide excellent flow measurement accuracy since it is estimated at ± 3% provided the device functions under free-flow conditions. However, this excellent accuracy is only obtained if the ratio of flow depth h_1 at the measuring point to the length L of the device is in the range [0.10; 0.40]. Outside this range, inaccuracies are observed, which are attributed to the increase in the approach flow velocity associated with the resulting

disturbances of the free water surface and its rapid changes. For this reason, most cutthroat flumes have been designed so that the ratio h_1/L is on the order of 1/3, which is a value belonging to the recommended aforementioned range.

The stage-discharge relationship for the cutthroat flume has been expressed as follows: $Q = C\, h_1^n$, where C is the calculated flume discharge constant varying by flume length/throat width/units, and n is the discharge exponent, which depends upon the flume size. Notably, the value of the exponent n greatly exceeds the legitimate 3/2 value of the rectangular sections.

The aforementioned devices are the oldest flumes developed during the 1960s; nevertheless, despite their age, these are the main flumes used today in many different applications, such as irrigation canals and stream gauging. Notably, these devices are insufficiently developed from a theoretical point of view. However, this observation can also be made in recently developed flumes, which remain all the same promising devices. This is the case for SM-Flume (Samani and Magallanez, 2000), which bears the initials of its authors, circular flumes (Samani et al., 1991) allowing the measurement of a wide range of discharges with great accuracy. For this device, the flow rate is a function of the total load to a power of 2.31, a value that is somewhat close to 2.5 corresponding to the V-Notch (Bos, 1976; Bos, 1989). Thus, it has been concluded by some authors, in a hasty way to say the least, that the circular flume creates an effect similar to that of V-Notch (Samani et al., 1991). Among recent devices, it is worth referring to the so-called central baffle flume (Kolavani et al., 2019; Bijankhan and Ferro, 2019; Aniruddha et al., 2020). In 2016, Ferro proposed a theoretical stage-discharge relationship for a central baffle flume using dimensional analysis. This relationship has been calibrated based on Peruginelli and Bonacci's experimental results (Perruginelli and Bonacci, 1997). Additionally, the effect of different geometrical parameters of a central baffle flume was experimentally observed by Kolavani et al. (2019), Bijankhan and Ferro (2019), and Aniruddha et al. (2020).

The above listed devices are, for the most part, made up of a rectangular section for which an acceptable accuracy is obtained only for high flow rates. The triangular section offers excellent accuracy for both low and high flows, as shown by authors in the recent past (Achour and Amara, 2022) while considering a triangular broad-crested weir as a measurement device.

Therefore, the present research examines the possibility of exploiting the performances of the triangular section in the flow measurement using a new type of flume. The principle adopted consists of designing a triangular section flowmeter, with a variable vertex angle depending on the length, ensuring a lateral contraction of the sidewalls. This is the converging section of the device to which a throat is added. Inevitably, the walls of the device are curved; hence, the name "Curved Wall Triangular Flume" is abbreviated as CWTF.

What is expected at first is to define the dimensions of the device using exclusively indisputable geometrical considerations. To provide the designer with dimensionless practical relationships, the dimensions of the device are related to the top width of the approach channel, which is a given parameter for a given installation.

In a second step, we plan to derive the stage-discharge relationship, hence that of the discharge coefficient, by theoretical considerations based on simple principles of fluid mechanics. These theoretical relationships will be validated or refined through an intense experimental program involving eight devices with different geometries tested in an appropriate installation.

MATERIAL AND METHODS

Description of the device and the resulting flow

Fig. 1 shows a plan view of the device emplaced in an approach channel of trapezoidal cross-section of bottom width b_o and top width B_o, for which flow rate measurement is needed. As the channel is an already built structure, all its geometrical parameters are known. These parameters are indicated by an "o" subscript, such as the height h_o or the side slopes m_o horizontal to 1 vertical, as shown in Fig. 2, representing the half diagram in accordance with section M-M shown in Fig. 1.

In Fig. 1, the device has been deliberately designated by the letters "DEVICE'". It is thus composed of two static parts, namely, the converging sections "DECE'" and the throat "EVIC". All cross sections of the device are triangular. In the converging sections, the apex angle decreases from θ to α (Fig. 2), resulting in curved walls DEGF and E'CGF. The inlet top width B of the device is represented by DE', and the outlet top width b is designated by EC, which is also the top width of the throat. Thus, as in most existing flumes, the CWTF is based on the contraction of its sidewalls.

The throat is a short channel of triangular cross-section with a constant opening angle α along its entire length EV (Fig. 1). As a rule, the length of the throat is determined based on existing assistive devices, preliminarily calibrated devices, or experimental observations. However, the throat must be long enough to cause parallel flow lines in the control section, which will properly assume its role as the specific flow control region producing the stage-discharge relationship.

The device is devoid of the diverging section, known as discharge sections, which is reminiscent of the modified Parshall flume, well-known as the USGS portable flume [6], but with triangular cross sections. With the deletion of the discharge sections, the device requires free-spilling flow off the end, i.e., in section V-I (Fig. 1).

As shown in Fig. 1, the apparatus is generated by two circles (C1) and (C2) of radii R_1 and R_2, respectively, both tangent to each other at point D and at points E and S to the horizontal line passing through points V and E belonging to the crest of the throat. The

straight line, which passes along the upper crest of the wall of the trapezoidal channel, is tangent to the circle (C2) at point P. It is easy to show that the horizontal distance ES (Fig. 1) is equal to $2\sqrt{R_1 R_2}$.

For a given installation, regardless of the contraction rate $\beta = b/B$ and angle ϕ, Fig. 1 allows us to geometrically write the following:

$$B = \frac{1 - 0.5(1 - \cos\phi)}{1 - 0.5\beta\,(1 - \cos\phi)} B_o \tag{1}$$

In other words, for a given installation, one may write rightly what follows:

$$B = \varepsilon\, B_o \tag{2}$$

where ε is a constant, less than unity, solely depending on the geometrical characteristics of the given installation as follows:

$$\varepsilon = \frac{1 - 0.5(1 - \cos\phi)}{1 - 0.5\beta\,(1 - \cos\phi)} \tag{3}$$

For a chosen angle ϕ, ε is solely dependent on the contraction rate β of the device according to Eq. (3). Choosing the appropriate angle ϕ is momentous in ensuring a smooth transition between the device and the approach channel providing flow without any disturbance. In Figs. 1 and 2, the transition, providing the connection between the approach channel and the inlet section of the device, is represented by the arc PD belonging to circle (C2). Typically, the design of the transition between channels and flumes is somewhat complicated since it is based on the principles of energy and momentum conservation (Chow, 1959). In the current case, it will be well defined by geometrical considerations, which is the easiest method since the transition is defined by an arc of a circle (Figs. 1, 3) whose appropriate central angle ϕ will be selected, according to the recommendation of the literature and the authors' observations.

Table 1 gives the values of ε according to Eq. (3), for some angles ϕ and contraction rates β. For a given value of β, ε increases with increasing angle ϕ, meaning that B approaches B_o. In other words, the length of the arc PD ensuring the transition between the device and the approach channel decreases accordingly (Fig. 1). The particular configuration of the device corresponds to the case where the length of the arc PD is deleted, meaning that the contraction rate of the device is $\beta_o = b/B_o$.

Table 1: Values of ε according to Eq. (3)

β	$\phi = 20°$	$\phi = 25°$	$\phi = 30°$	$\phi = 45°$
	ε	ε	ε	ε
0.10	0.9727796	0.95764006	0.93930485	0.86623917
0.15	0.97425291	0.95989902	0.94248286	0.87272452
0.20	0.97573069	0.96216866	0.94568244	0.87930772
0.25	0.97721295	0.96444906	0.94890383	0.88599098
0.30	0.97869973	0.9667403	0.95214723	0.89277662
0.35	0.98019104	0.96904245	0.95541289	0.899667
0.40	0.9816869	0.97135558	0.95870102	0.90666457
0.45	0.98318734	0.97367979	0.96201186	0.91377185
0.50	0.98469236	0.97601515	0.96534565	0.92099143
0.55	0.98620201	0.97836173	0.96870263	0.928326
0.60	0.98771628	0.98071963	0.97208303	0.93577833
0.70	0.99075883	0.98546969	0.97891512	0.9510478
0.80	0.99382019	0.99026598	0.98584392	0.96682385

From a geometrical point of view, Fig. 2 allows us to write the following:

$$\tan(\theta/2) = m_1 = \frac{B}{2h_o} \tag{4}$$

Hence,

$$\theta = 2\tan^{-1}\left(\frac{B}{2h_o}\right) \tag{5}$$

For the device configuration corresponding to $B = B_o$, the angle θ is then maximal, and Eq. (5) becomes the following:

$$\theta_{\max} = 2\tan^{-1}\left(\frac{B_o}{2h_o}\right) \tag{6}$$

Eq. (6) allows a fast calculation of the maximal opening angle of the inlet section of the device, provided the top width B_o and the height h_o of the device are given, which is the case in practice. Before choosing the appropriate angle for the inlet section of the device, it is useful to calculate the maximum angle not to exceed, according to Eq. (6).

Similarly, Fig. 2 allows us to geometrically write the following:

$$\tan(\alpha/2) = m_2 = \frac{b}{2h_o} \tag{7}$$

Hence,

$$\alpha = 2\tan^{-1}\left(\frac{b}{2h_o}\right) \tag{8}$$

Additionally, the ratio of Eq. (7) to Eq. (4) results in the following:

$$\frac{m_2}{m_1} = \frac{b}{B} = \beta \tag{9}$$

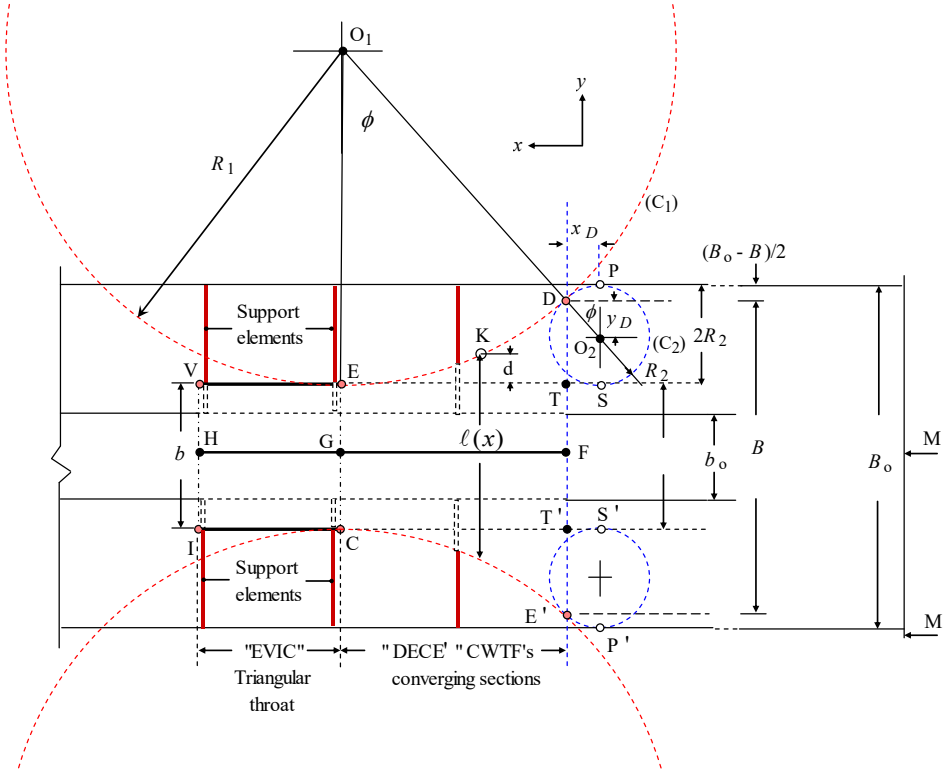

Figure 1: Plan view of the device represented by "DEVICE'" inserted into a trapezoidal approach channel of top width B_o and base width b_o

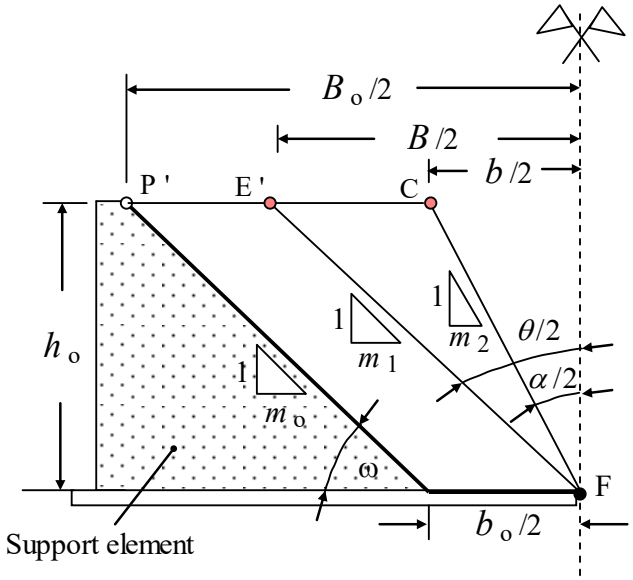

Figure 2: View of section M-M according to Fig. 1

Fig. 3 shows details of the generating circle (C2) of center O_2, adopting the same notations as those of Fig. 1. The parameters of the circle (C2) will be useful for drawing the second generator circle (C1) with center O_1tangent at both points E and D.

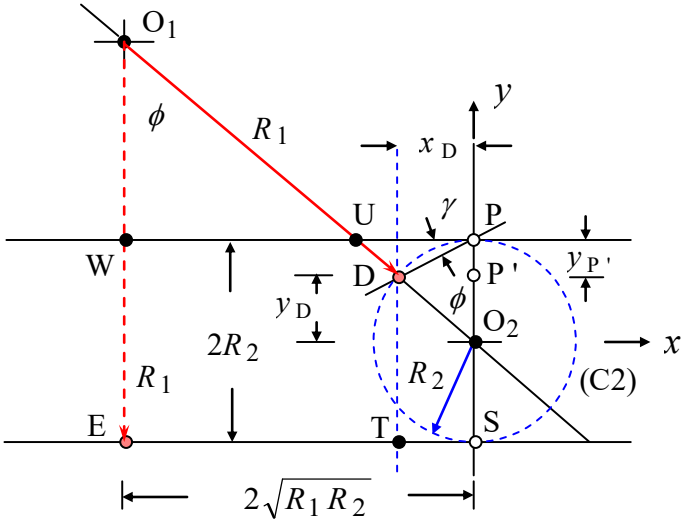

Figure 3: Geometric parameters of the generating circle (C2) according to Fig. 1, including notations

With the help of Fig. 1, the following relationships can be derived from geometrical considerations:

$$R_2 = \frac{1}{4}(B_o - b) \tag{10}$$

Considering Eq. (2), Eq. (10) can be rewritten as follows:

$$R_2 = \frac{1}{4}B(\varepsilon^{-1} - \beta) \tag{11}$$

Dividing both sides of Eq. (11) by B_o and considering Eq. (2) results in the following:

$$\frac{R_2}{B_o} = \frac{1}{4}\varepsilon(\varepsilon^{-1} - \beta) \tag{12}$$

Eq. (12) is reduced to the following:

$$\frac{R_2}{B_o} = \frac{1}{4}(1 - \varepsilon\beta) \tag{13}$$

Given Eq. (2), Eq. (3) indicates that the ratio R_2/B_o only depends on the contraction rate β of the device for a given angle ϕ. Typically, the contraction rate β of the device and the angle ϕ are chosen, which allows a forthwith calculation of the radius R_2 according to Eq. (13) since the top with B_o of the approach channel is given data. Once the radius R_2 has been determined, its graphical representation at a chosen scale is easy.

Additionally, it is required to place point D on circle (C2), represented in Figs. (1) and (3), by adopting the following precise coordinates:

$$y_D = R_2 \cos\phi \tag{14}$$

Considering the top width B_o as a reference length, Eq. (14) is then rewritten as follows:

$$\frac{y_D}{B_o} = \frac{R_2}{B_o}\cos\phi \tag{15}$$

Considering Eq. (13), Eq. (15) reduces to the following:

$$\frac{y_D}{B_o} = \frac{1}{4}(1 - \varepsilon\beta)\cos\phi \tag{16}$$

Similarly, one may write the following:

$$x_D = R_2 \sin\phi \tag{17}$$

Eq. (17) can be rewritten as follows:

$$\frac{x_D}{B_o} = \frac{R_2}{B_o} \sin\phi \tag{18}$$

Eliminating the ratio R_2/B_o between Eqs. (13) and (18) yields the following:

$$\frac{x_D}{B_o} = \frac{1}{4}(1-\varepsilon\beta)\sin\phi \tag{19}$$

For a given or projected installation, for which angle ϕ has been chosen, the coordinates y_D and x_D can be determined using Eqs. (16) and (19), respectively, since both β and B_o are provided data.

Considering Fig. 2, the top width B_o of the trapezoidal approach channel is as follows:

$$B_o = b_o + 2m_o h_o \tag{20}$$

where:

$$m_o = \cot\omega \tag{21}$$

The vertical distance $\overline{PP'}$ is such that:

$$\overline{PP'} = y_{P'} = R_2 - y_D \tag{22}$$

One may rewrite Eq. (21) as follows:

$$\frac{\overline{PP'}}{B_o} = \frac{R_2}{B_o} - \frac{y_D}{B_o} \tag{23}$$

With the help of Eqs. (13) and (16), Eq. (23) reduces to the following:

$$\frac{\overline{PP'}}{B_o} = \frac{1}{4}(1-\varepsilon\beta)(1-\cos\phi) \tag{24}$$

Additionally, one may observe in Fig. 3 that the triangle ΔDPO_2 is isosceles, allowing us to write the following:

$$\angle O_2DP = \angle O_2PD = \frac{\pi - \phi}{2} \tag{25}$$

Hence, the angle γ is expressed as follows:

$$\angle \gamma = \frac{\pi}{2} - \frac{\pi - \phi}{2} \tag{26}$$

That is,

$$\angle \gamma = \frac{\phi}{2} \tag{27}$$

With Eqs. (19), (24), and (27), the geometry of the transition between the approach channel and the flume is well defined provided β, ϕ, and B_o are given; this is the arc of a circle PD (Fig. 1, 2), which is written as follows:

$$\mathrm{PD} \cap = R_2 \, \phi \tag{28}$$

where the angle ϕ is expressed in radians.

Eq. (28) can be rewritten as follows:

$$\frac{\mathrm{PD} \cap}{B_o} = \frac{R_2}{B_o} \phi \tag{29}$$

Inserting Eq. (13) into Eq. (29) results in the following:

$$\frac{\mathrm{PD} \cap}{B_o} = \frac{1}{4} (1 - \varepsilon \beta) \phi \tag{30}$$

Considering the triangle $\Delta O_1 WU$, one may write the following:

$$\tan \phi = \frac{\overline{\mathrm{WU}}}{\overline{\mathrm{WO}_1}} = \frac{2\sqrt{R_1 R_2} - R_2 \tan \phi}{R_1 - 2R_2} \tag{31}$$

Calculations show that Eq. (31) is a second-degree equation that is written as follows:

$$R_1^2 - 2\left(\frac{2 + \tan^2 \phi}{\tan^2 \phi}\right) R_2 R_1 + R_2^2 = 0 \tag{32}$$

Among the two solutions of Eq. (32), one must retain the one that satisfies the inequality $R_1 > R_2$. Hence, the sought solution is:

$$R_1 = \left[\left(\frac{2 + \tan^2 \phi}{\tan^2 \phi}\right) + \sqrt{\left(\frac{2 + \tan^2 \phi}{\tan^2 \phi}\right)^2 - 1}\right] R_2 \tag{33}$$

Eq. (33) shows that the ratio R_1/R_2 is a constant for a given angle ϕ. Eq. (33) can be rewritten as follows:

$$\frac{R_1}{B_o}=\left[\left(\frac{2+\tan^2\phi}{\tan^2\phi}\right)+\sqrt{\left(\frac{2+\tan^2\phi}{\tan^2\phi}\right)^2-1}\right]\frac{R_2}{B_o} \qquad (34)$$

Eliminating the ratio R_2/B_o between Eqs. (13) and (34) results in the following:

$$\frac{R_1}{B_o}=\frac{1}{4}\left[\left(\frac{2+\tan^2\phi}{\tan^2\phi}\right)+\sqrt{\left(\frac{2+\tan^2\phi}{\tan^2\phi}\right)^2-1}\right](1-\varepsilon\beta) \qquad (35)$$

Since β, B_o, and ϕ are given, Eq. (35) explicitly gives the value of radius R_1, allowing us to draw circle (C1), as shown in Fig. 1.

According to Fig. 3, the length $\overline{\mathrm{ET}}$ of the device's converging sections, which are also shown in Fig. 1, is expressed as follows:

$$\overline{\mathrm{ET}}=2\sqrt{R_1 R_2}-x_D \qquad (36)$$

Eq. (36) can be rewritten as follows:

$$\frac{\overline{\mathrm{ET}}}{B_o}=2\sqrt{\frac{R_1 R_2}{B_o^2}}-\frac{x_D}{B_o} \qquad (37)$$

With the help of Eqs. (13), (19), and (35), Eq. (36) reduces to the following:

$$\frac{\overline{\mathrm{ET}}}{B_o}=\frac{1}{2}\left\{\left[\left(\frac{2+\tan^2\phi}{\tan^2\phi}\right)+\sqrt{\left(\frac{2+\tan^2\phi}{\tan^2\phi}\right)^2-1}\right]^{1/2}-\frac{1}{2}\sin\phi\right\}(1-\varepsilon\beta) \qquad (38)$$

Eq. (38) allows a fast and exact calculation of the appropriate length of the device's converging sections, provided β, B_o, and ϕ are given.

Regarding the top width b of the throat, Eq. (1) can be rewritten as follows:

$$\frac{B}{b}=\frac{1-0.5(1-\cos\phi)}{1-0.5\beta\,(1-\cos\phi)}\left(\frac{B_o}{b}\right) \qquad (39)$$

After rearrangement, Eq. (39) reduces to the following:

$$\frac{b}{B_o} = \beta \frac{1 - 0.5(1 - \cos\phi)}{1 - 0.5\beta\,(1 - \cos\phi)} \tag{40}$$

That is,

$$\frac{b}{B_o} = \varepsilon\,\beta \tag{41}$$

Furthermore, consider the orthogonal axis system EO_1ET (Fig. 1), where EO_1 is the Y-axis and ET is the X-axis. In this system, the vertical distance d (Fig. 1) varies from d = 0 at x = 0 (Point E) to d = $\overline{TD}$ at x = $\overline{ET}$. Additionally, the top width $\ell(x)$ of the converging sections (Fig. 1), which varies from b to B in the direction of the X-axis, can be written as follows:

$$\ell(x) = b + 2d \tag{42}$$

Considering the point K(x, d) belonging to the circle (C1) (Fig. 1), one may write the following equation:

$$x^2 + (R_1 - d)^2 = R_1^2 \tag{43}$$

After some arrangements, Eq. (43) reduces to the following:

$$\frac{d}{R_1} = 1 - \sqrt{1 - \left(\frac{x}{R_1}\right)^2} \tag{44}$$

Combining Eqs. (41), (42) and (44) results in the following nondimensional relationship:

$$\frac{\ell(x)}{B_o} = \varepsilon\beta + 2\frac{R_1}{B_o}\left(1 - \sqrt{1 - \left(\frac{x/B_o}{R_1/B_o}\right)^2}\right) \tag{45}$$

Eq. (45) is very useful since it allows calculating the top width of the converging sections of the device at any point of abscissa x belonging to the arc of circle DE $\cap$ and whose value will be chosen by the designer over the entire distance $\overline{ET}$ (Fig. 1). The ratio R_1/B_o is easily computed according to Eq. (35) since the contraction rate β and the angle ϕ are given.

The aforementioned relationships, derived from geometrical considerations, give the linear dimensions of the device's converging sections with precision, including the apex angles of the inlet and the outlet sections, provided some parameters are given, most

notably the angle ϕ. Additionally, all the required geometrical characteristics of the device are related to the top width B_o of the approach channel, the value of which is known for a given installation.

As has already been indicated, to ensure a regular flow without any disturbance or detachment from walls, the choice of the angle ϕ should not be made at random. Several geometrical representations plotted at various scales show that the optimum value of the angle ϕ is 45°. According to the authors' experimental observations, $\phi = 45°$ also ensures a smooth transition between the inlet section of the device and the approach channel through the arc PD of the circle (C2), as shown in Figs. 1 and 3. Moreover, with $\phi = 45°$, it was observed that the arc length PD is short enough to rightly neglect, on the one hand, linear head losses and, on the other hand, minor head losses due to the relatively low values of the $\varepsilon = B/B_o$ contraction rate, as highlighted in Table 1.

For the purposes of the tests, the various scale models involved will be built on the basis of ϕ = 45° after choosing a value of the contraction rate β. Thus, the required linear dimensions will be obtained by introducing the values of these two parameters into the previously established theoretical relationships. Details of the geometry of the CWTFs involved in the experimental tests will be disclosed in the appropriate section of the paper.

With regard to the behavior of the resulting flow, as a restricting structure, the device accelerates flow through the converging sections DECE', shown in Fig. 1, from the slow subcritical state in the inlet to the supercritical state in the throat "EVIC", creating a critical state flow between them expected to be in section EC or in a section located only slightly further downstream inside the throat. Due to its converging sections, the flow depth decreases inside the CWTF from depth h_1 to critical depth $h_{2,c}$, as shown in Fig. 4.

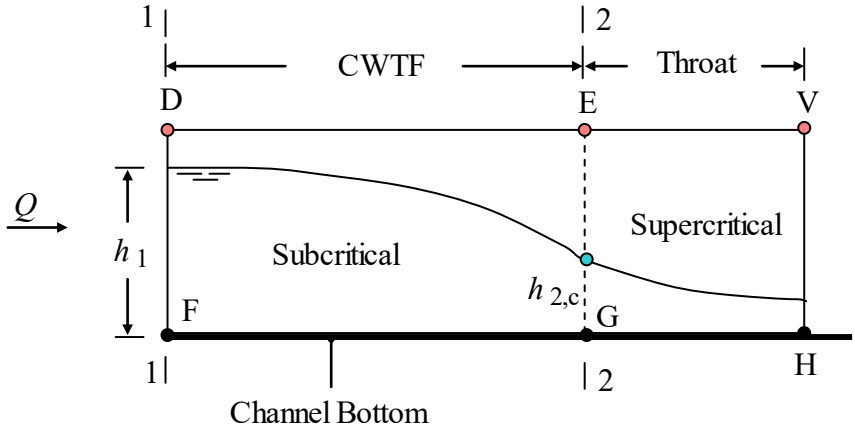

Figure 4: Longitudinal flow profile inside the device. Notations according to Fig. 1

The control section located at section 2-2 appears despite the device having no change in bottom elevation. This is the *sine qua non* condition of the correct functioning of the device under consideration, thus developing a unique relationship between the upstream water level and the flow rate Q. This means, from a mathematical point of view, that the discharge is a single-valued function of the upstream flow depth h_1, which is read in the inlet section of the device, i.e., section DE' shown in Fig. 1 corresponding to section DF of Fig. 3.

The throat must be long enough to cause parallel flow lines in the control section, which will properly assume its role as the specific flow control region producing the stage-discharge relationship.

Dimensional analysis and discharge coefficient dependency

To derive the functional relationship relating the discharge coefficient C_d of the device to the physical parameters involved in the resulting flow, dimensional analysis is the most appropriate method. The discharge coefficient C_d is the ratio of the actual flow rate to the theoretical flow rate. Thus, the discharge coefficient can be thought of as a correction factor of the flow rate and hence a correction factor of flow meter devices. It is commonly derived from laboratory tests for each device; however, for some flow measurement devices, the theory was able to derive the C_d governing relationship, which is solely dependent on the geometrical characteristics of the device. Thus, to find the sought functional C_d relationship using dimensional analysis, it is first required to identify all the parameters that affect the flow rate Q passing through the device under consideration. These are manifestly the flow depth h_1 at the inlet of the device (Fig. 4), the apex angle θ of the inlet triangular cross section DE' of the device (Figs. 1, 2), the apex angle α of the outlet triangular cross section EC of the device (Figs. 1, 2), the length L = ET = GF of the device's converging sections (Figs. 1, 3), the acceleration g due to gravity, the density ρ of the flowing liquid, the dynamic viscosity μ of the flowing liquid, and the surface tension σ.

The nine aforementioned parameters can be related to each other by the following functional relationship:

$$f\left(Q,\rho,g,h_1,L,\mu,\sigma,\theta,\alpha\right)=0 \tag{46}$$

Using the Vashy-Buckingham π theorem (Langhaar, 1962), one may derive the following new functional relationship encompassing the involved dimensionless variables:

$$\lambda\left(\frac{Q}{g^{1/2}h_1^{5/2}},\frac{\rho g^{1/2}h_1^{3/2}}{\mu},\frac{\rho g h_1^2}{\sigma},\frac{h_1}{L},\theta,\alpha\right) \tag{47}$$

Hence, it is easy to recognize the Reynolds number R_e and the Weber number W as being the second and third terms between the brackets of the functional relationship (47), respectively. Thus, Eq. (47) reduces to:

$$\frac{Q}{g^{1/2} h_1^{5/2}} = \psi \left(R_e, W, \frac{h_1}{L}, \theta, \alpha \right) \tag{48}$$

However, choosing the top width B of the inlet section of the device as a reference linear dimension influencing the discharge Q for a given installation, the ratio h_1/L can be written as follows:

$$\frac{h_1}{L} = \frac{h_1 / B}{L / B} \tag{49}$$

Considering Eq. (2), Eq. (49) becomes the following:

$$\frac{h_1}{L} = \frac{h_1 / B_o}{L / B_o} \tag{50}$$

The influence of the L/B_o ratio on the discharge is nonexistent since it is a constant for a device of a given size. Flow rates Q passing through this device are in no way affected. Additionally, the angles θ and α are related to the side slopes m_1 and m_2 according to Eqs. (4) and (7), respectively. Moreover, the ratio m_2/m_1 was determined to be the contraction rate β of the device in accordance with Eq. (9). The flow through the device is in the turbulent state, and the Reynolds number R_e can then be neglected. Surface tension effects represented by the Weber number W are only prominent at very low flow rates and very narrow opening angles θ and α; these effects are negligible given the practical hydraulic conditions considered in the current study.

Thus, considering the relevant previous considerations, Eq. (48) is reduced to:

$$\frac{Q}{m_1 g^{1/2} h_1^{5/2}} = \zeta \left(\frac{h_1}{B_o}, \beta \right) \tag{51}$$

Eq. (51) is in the form of the well-known discharge relationship governing weirs, allowing us to derive the discharge coefficient C_d as follows:

$$C_d = \zeta \left(\frac{h_1}{B_o}, \beta \right) \tag{52}$$

It can thus be observed, as in the case of all devices based on the lateral contraction of their sidewalls, the dependency of the discharge coefficient C_d on the contraction rate β, which is expected to be strong. In one of the appropriate sections of the paper, the theory

will confirm this dependence. However, the theory will not be able to show the influence of the relative depth h_1/B_o on the discharge coefficient C_d. For this, only the analysis of the experimental data can confirm or invalidate this influence and for which range of β.

Theoretical discharge and discharge coefficient relationships

Use of the energy equation

Given the triangular shape, the critical depth $h_{1,c}$ in inlet section 1-1 of the device (Fig. 4) can be written as follows:

$$h_{1,c} = \left(\frac{2Q^2}{g m_1^2} \right)^{1/5} \tag{53}$$

where the subscript "*c*" denotes the critical condition.

Similarly, the critical depth $h_{2,c}$ in triangular section 2-2 (Fig. 4) is written as follows:

$$h_{2,c} = \left(\frac{2Q^2}{g m_2^2} \right)^{1/5} \tag{54}$$

The ratio of Eq. (53) to Eq. (54) results in the following relationship after performing some simplifications:

$$\left(\frac{h_{1,c}}{h_{2,c}} \right)^5 = \left(\frac{m_2}{m_1} \right)^2 \tag{55}$$

Considering Eq. (9) and rearranging Eq. (55) reduces to the following:

$$h_{1,c} = h_{2,c} \beta^{2/5} \tag{56}$$

Additionally, neglecting the head loss between the inlet 1-1 and outlet 2-2 sections of the device, one may write the following:

$$H_1 = H_2 = \frac{5}{4} h_{2,c} \tag{57}$$

where H_1 and H_2 are the total heads in triangular sections 1-1 and 2-2, respectively. Thus, we can deduce the following:

$$h_{2,c} = \frac{4}{5} H_1 \tag{58}$$

Inserting Eq. (58) into Eq. (56) yields the following:

$$h_{1,c} = \frac{4}{5} H_1 \beta^{2/5} \tag{59}$$

Let us define the following dimensionless parameter, representing the relative total head in section 1-1 (Fig. 4):

$$H_1^* = \frac{H_1}{h_{1,c}} \tag{60}$$

Thus, Eq. (59) is reduced to the following:

$$H_1^* = \frac{5}{4} \beta^{-2/5} \tag{61}$$

For a given constructed device, characterized by a well-defined contraction rateβ, Eq. (61) shows that the dimensionless parameter H_1^* is constant regardless of the flow rate Q or the flow depth h_1. This is an intrinsic feature of the device that could be attributed to its particular shape.

Additionally, considering the effect of the approach flow velocity, the total head H_1 in inlet section 1-1 of the device (Fig. 4) is written as follows:

$$H_1 = h_1 + \frac{Q^2}{2 g A_1^2} \tag{62}$$

where A_1 is the water area of triangular section 1-1, which is expressed as follows:

$$A_1 = m_1 h_1^2 \tag{63}$$

Inserting Eq. (63) into Eq. (62) results in the following:

$$H_1 = h_1 + \frac{Q^2}{2 g m_1^2 h_1^4} \tag{64}$$

Combining Eqs. (53), (12), and (64), the following final result is derived:

$$H_1^* = h_1^* + \frac{1}{4 h_1^{*4}} \tag{65}$$

where the relative initial flow depth h_1^* is defined as:

$$h_1^* = \frac{h_1}{h_{1,c}} \tag{66}$$

Inserting Eq. (61) into Eq. (65) results in the following:

$$h_1^* + \frac{1}{4h_1^{*4}} = \frac{5}{4}\beta^{-2/5} \tag{67}$$

After rearrangement, Eq. (67) is reduced to the following fifth-degree equation:

$$h_1^{*5} - \frac{5}{4}\beta^{-2/5} h_1^{*4} + \frac{1}{4} = 0 \tag{68}$$

Eq. (68) is implicit in h_1^*, whose value is well defined for a known contraction rate β. For the case of H_1^*, the initial relative depth h_1^* is a constant for a designed device characterized by a given contraction rate β, regardless of the flow rate Q or the flow depth h_1. Additionally, among the solutions of Eq. (68), the only appropriate one to retain should meet the requirement $h_1^* > 1$ since the flow in section 1-1 is subcritical corresponding to $h_1 > h_{1,c}$.

Based on an iterative process applied to the implicit Eq. (68), Table 2 gives exact values of h_1^* as a function of β varying in the wide range [0.15; 0.80]. As seen, h_1^* decreases as β increases, and their variation is shown in Fig. 5, in accordance with the values reported in Table 2.

Table 2: Values of the relative initial depth h_1^* as a function of the contraction rate β, according to Eq. (68)

β	h_1^*
0.15	2.66481027
0.20	2.37166562
0.25	2.16499724
0.30	2.00792598
0.35	1.88240587
0.40	1.77838057
0.45	1.68971437
0.50	1.6123977
0.55	1.54365857
0.60	1.48148031
0.65	1.42431687
0.70	1.37090674
0.75	1.32013003
0.80	1.27086296

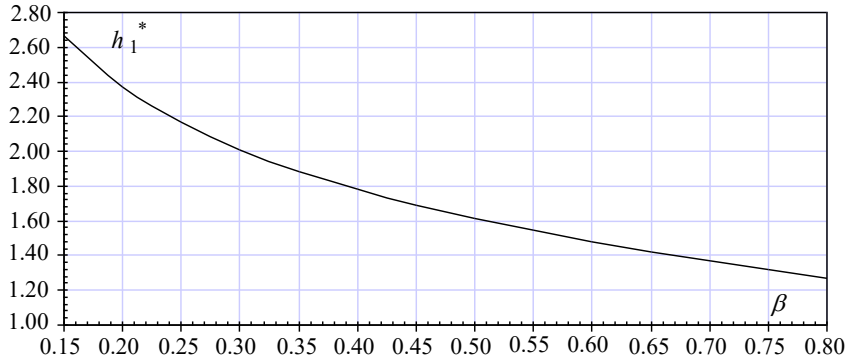

Figure 5: Variation in the relative initial depth h_1^* as a function of the contraction rate β, according to values reported in Table 1

As will be seen later, the relative depth h_1^* plays a determining role in the calculation of the sought discharge coefficient C_d of the device. Thus, its value must be as accurate as possible to minimize the relative error in the C_d calculation.

The exact value of h_1^* can be determined by an iterative process applied to Eq. (68), carried out with a machine such as modern pocket calculators in which a powerful solver is incorporated. The iterative calculation can also be performed successfully using the Excel solver. The best way of speeding up the convergence of the iteration would be to introduce an appropriate initial value $h_{1,0}^*$, as close as possible to the exact value, into the calculation process. Intense calculations showed that the best value of $h_{1,0}^*$ could be obtained by the Hoerl model, which is often used for curve fitting purposes (Kolb, 1983). Thus, according to this model, the following improved $h_{1,0}^*(\beta)$ explicit relationship was derived:

$$h_{1,0}^* = 1.454 \left(0.772^{\beta}\right) \beta^{-0.337} \tag{69}$$

Within the wide range $0.15 \leq \beta \leq 0.80$, the maximum deviation between the approximate Eq. (69) and the exact Eq. (68) is less than 0.53%. Additionally, if the designer prefers using the handy approximate Eq. (69) to avoid the constraining iterative process required in solving the implicit Eq. (68), then, a maximum relative error of less than 1.33% will be committed in the calculation of discharge coefficient C_d, and hence on the flow rate Q. In practice, this relative maximal error is quite acceptable, and therefore, the use of the approximate Eq. (69) can be envisioned with great confidence in the range of validity $0.15 \leq \beta \leq 0.80$.

The discharge Q is expressed by Eq. (53) as follows:

$$Q = \frac{1}{2}\sqrt{2g}\, m_1\, h_{1,c}^{5/2} \tag{70}$$

Considering both Eqs. (9) and (66), Eq. (70) reduces to the following:

$$Q = \frac{1}{2}\beta^{-1} h_1^{*-5/2} \sqrt{2g} m_2 h_1^{5/2} \tag{71}$$

Eq. (71) is in the form of the stage-discharge relationship governing semimodular triangular shaped flow meters and weirs used for open channel flow measurement, allowing us to derive the sought discharge coefficient C_d of the considered device as follows:

$$C_d = \frac{1}{2}\beta^{-1} h_1^{*-5/2} \tag{72}$$

Considering Eq. (68), Eq. (72) shows that the discharge coefficient C_d of the device is solely dependent on the contraction rate β. Eq. (72) gives no indication of a possible influence of the upstream relative depth on the discharge coefficient.

Additionally, considering Eq. (69), one may derive the following explicit approximate discharge coefficient relationship:

$$C_d = 0.196\beta^{-0.157}\left(0.77^{-5\beta/2}\right) \tag{73}$$

The maximum deviation between approximate Eq. (73) and Eq. (72), involving exact values of h_1^* according to Eq. (68), is only 1.266%

Table 3 groups together the calculated discharge coefficients for some contraction rates according to Eq. (72) along with Eq. (68); this allowed plotting Fig. 6 showing the variation in C_d as a function of β.

Table 3: Values of the discharge coefficient C_d of the device for some given contraction rates β according to Eq. (72) along with Eq. (68)

β	C_d
0.15	0.28754976
0.20	0.28860667
0.25	0.28999241
0.30	0.29172893
0.35	0.29384533
0.40	0.29637956
0.45	0.29938101
0.50	0.30291416
0.55	0.30706421
0.60	0.31194573
0.65	0.31771674
0.70	0.32460274
0.75	0.33294076
0.80	0.34326791

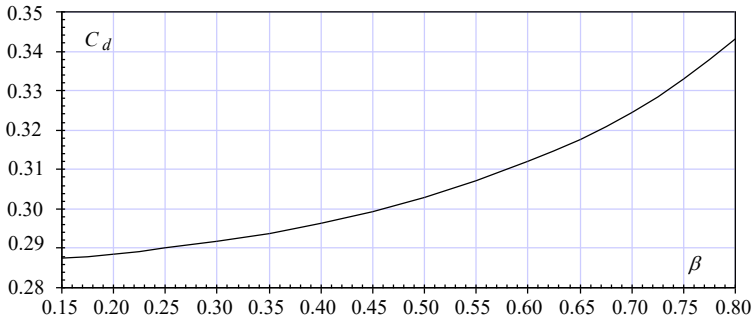

Figure 6: Variation in the discharge coefficient C_d with the contraction rate β of the device according to Table 3

The discharge coefficient C_d of the device increases with increasing contraction rate β, which is fully justified from a physical point of view. For a given value of the top width B of the inlet section of the device, the contraction rate β increases when the top width b of the outlet section of the device increases; this helps to improve the conveying of the flow through the throat resulting from a greater discharge coefficient.

Use of the kinetic factor

In this section, we put forward an approach that is as rigorous and reliable as the first, intending to derive the theoretical stage-discharge relationship and hence that governing the discharge coefficient of the device. The effect of the approach flow velocity is carefully included in this method.

The velocity head in section 1-1 (Fig. 4) is deliberately written as a fraction δ of the flow depth h_1 in terms of the mean velocity V_1. Thus, considering the Coriolis coefficient equal to unity, one may write the following:

$$\frac{V_1^2}{2g} = \delta h_1 \tag{74}$$

This results in writing the initial total head H_1 as follows:

$$H_1 = h_1 + \frac{V_1^2}{2g} = (1+\delta)h_1 \tag{75}$$

The dimensionless parameter δ can be deservedly considered a kinetic factor. It varies between 0 and 1 while remaining strictly less than 1 due to the subcritical nature of the flow in section 1-1. When the total head H_1 merges with the flow depth h_1, the kinetic factor $\delta \to 0$ in full accordance with Eq. (75).

Considering the continuity equation $V_1 = Q/A_1$, where $A_1 = m_1 h_1^2$ in the water area in section 1-1 (Fig. 4), Eq. (74) allows us to write the kinetic factor δ as follows:

$$\delta = \frac{Q^2}{2g\, m_1^2\, h_1^5} \tag{76}$$

Combining Eqs. (53), (59), and (75) results in the following:

$$Q^2 = \frac{1}{2}\left(\frac{4}{5}\right)^5 g\, m_1^2\, \beta^2 \left(1+\delta\right)^5 h_1^5 \tag{77}$$

Inserting Eq. (77) into Eq. (75) and simplifying yields the following:

$$\delta = \frac{1}{4}\left(\frac{4}{5}\right)^5 \beta^2 \left(1+\delta\right)^5 \tag{78}$$

Hence,

$$\frac{\left(1+\delta\right)^5}{\delta} = 4\left(\frac{5}{4}\right)^5 \beta^{-2} \tag{79}$$

Eq. (79) reveals that the kinetic factor δ depends solely on the contraction rate β, which is then the approach flow velocity control parameter.

Let us denote C_o as the following constant:

$$C_o = 4\left(\frac{5}{4}\right)^5 \tag{80}$$

Thus, Eq. (79) is rewritten as follows:

$$\frac{\left(1+\delta\right)^5}{\delta} = C_o\, \beta^{-2} \tag{81}$$

Eq. (81) is an implicit relationship in δ.

Additionally, when considering Eq. (9), Eq. (77) can be rewritten as follows:

$$Q = \frac{1}{\sqrt{C_o}} \left(1+\delta\right)^{5/2} \sqrt{2g}\, m_2\, h_1^{5/2} \tag{82}$$

Eq. (82) is the stage-discharge relationship of the device in which the discharge coefficient C_d is expressed as follows:

$$C_d = \frac{1}{\sqrt{C_o}}\left(1+\delta\right)^{5/2} \tag{83}$$

Eq. (83) shows that if the approach flow velocity were to be neglected, i.e., $\delta \to 0$, then the discharge coefficient of the device would be constant, such as $C_d = 1/\sqrt{C_o} \approx 0.286$, regardless of the contraction rate value. However, this configuration does not represent realness except for devices with low contraction rates β, i.e., $\beta < 0.15$ according to Table 3, which is rarely considered in practice.

An iterative process was applied to the implicit Eq. (81), allowing computing the values of the kinetic factor δ in a wide range of contraction rates β. These are reported in Table 4, showing that δ is less than unity while increasing with increasing contraction rate β.

Table 4: Values of the kinetic factor δ for some contraction rates β, computed according to Eq. (81)

β	δ	$\left(1+\delta\right)^{5/2}$
0.15	0.00186041	1.00465752
0.20	0.00333175	1.00835021
0.25	0.00525597	1.01319178
0.30	0.00765952	1.01925894
0.35	0.01057727	1.02665332
0.40	0.01405454	1.03550757
0.45	0.01814984	1.04599412
0.50	0.02293925	1.05833852
0.55	0.02852225	1.0728382
0.60	0.03503165	1.08989353
0.65	0.04264881	1.11005662
0.70	0.0516298	1.1341153
0.75	0.06235287	1.16324713
0.80	0.07541303	1.19932872

Table 4 reveals that if the approach flow velocity was not taken into consideration, then this would cause detrimental relative errors in the discharge coefficient calculation according to Eq. (83). As an example, considering the contraction rate $\beta = 0.45$, Table 4 shows that a relative error of 4.6% would be made in the calculation of C_d if the effect of the kinetic factor is neglected.

Additionally, since the kinetic factor δ is less than 1, the quantity $\left(1+\delta\right)^{5/2}$ in Eq. (81) is congruously expanded in a Taylor series up to the second order, resulting in the following quadratic relationship:

$$\delta^2 - \frac{1}{10}\left(C_o\,\beta^{-2} - 5\right)\delta + \frac{1}{10} = 0 \tag{84}$$

Eq. (84) is the so-called standard form of the quadratic equation in δ, having two distinct real roots, only one of which meets the requirement $\delta < 1$. It is expressed as follows:

$$\delta = \psi - \sqrt{\psi^2 - 0.1} \tag{85}$$

where:

$$\psi = \frac{1}{20}\left(C_o\,\beta^{-2} - 5\right) \tag{86}$$

Table 5 contrasts the exact δ values reported in Table 4 with the approximate values calculated according to Eq. (85) along with Eq. (86).

Table 5: Comparison between exact and approximate values of the kinetic factor δ computed using Eq. (81) and (85), respectively.

β	δ Exact Eq. (77)	δ Approximate Eq. (81)	Deviation (%)
0.15	0.00186041	0.00186041	6.0318E-06
0.20	0.00333175	0.00333175	3.709E-05
0.25	0.00525597	0.00525597	0.00014556
0.30	0.00765952	0.00765948	0.00045099
0.35	0.01057727	0.01057715	0.00119093
0.40	0.01405454	0.01405414	0.00280118
0.45	0.01814984	0.01814877	0.00589074
0.50	0.02293925	0.02293643	0.01227299
0.55	0.02852225	0.02851548	0.02372357
0.60	0.03503165	0.03501614	0.04427356
0.65	0.04264881	0.04261442	0.08064473
0.70	0.0516298	0.05155501	0.14486708
0.75	0.06235287	0.06219107	0.25948591
0.80	0.07541303	0.07505874	0.46979971

Table 5 confirms that the exact and approximate Eqs. (81) and (85), respectively, give very close values, meaning that Eq. (85) is very accurate. The maximum deviation is less than 0.47% obtained for the greatest value of the contraction rate, i.e., $\beta = 0.80$.

Inserting Eq. (85) into Eq. (83), the sought discharge coefficient relationship is expressed as follows:

$$C_d = \frac{1}{\sqrt{C_o}}\left(1 + \psi - \sqrt{\psi^2 - 0.1}\right)^{5/2} \tag{87}$$

Eq. (87) is the theoretical approximate relationship governing the discharge coefficient of the device derived from the kinetic factor method.

In the wide range $0.15 \leq \beta \leq 0.80$, the maximum deviation between the exact values of C_d given by Eq. (83) along with Eq. (81) and those computed using approximate Eq. (87) along with Eq. (86) is only 0.082%. This result shows that the discharge coefficient C_d can be calculated with excellent accuracy using the approximate Eq. (87).

Additionally, it is obvious that Eqs. (72) and (87), giving the discharge coefficient C_d, which has been deduced from the two methods previously described, should give the same result. Thus, the equality between the two equations allows us to write the following:

$$C_d = \frac{1}{2}\beta^{-1} h_1^{*\,-5/2} = \frac{1}{\sqrt{C_o}}\left(1+\psi-\sqrt{\psi^2-0.1}\right)^{5/2} \tag{88}$$

After simplifications and arrangements, the following final result is obtained:

$$h_1^* = \frac{5}{4}\beta^{-2/5}\left(1+\psi-\sqrt{\psi^2-0.1}\right)^{-1} \tag{89}$$

The maximum deviation between the exact values of h_1^* given by implicit Eq. (68) and approximate values given by Eq. (89), for the same contraction rate β, is less than 0.033%. This proves that Eq. (89) is highly reliable and accurate that the designer could use in Eq. (72).

Additionally, Eq. (82) governing the discharge Q becomes the following:

$$Q = \frac{1}{\sqrt{C_o}}\left(1+\psi-\sqrt{\psi^2-0.1}\right)^{5/2}\sqrt{2g}\, m_2\, h_1^{5/2} \tag{90}$$

Eq. (90) is the simplified form of the theoretical stage-discharge relationship that meets the requirements of semimodular devices.

This equation shows in particular the importance of the upstream depth h_1 in the calculation of the flow rate Q. The more precisely the upstream depth h_1 is measured, the greater the flow rate Q is determined with great reliability. In agreement with Eq. (90), a relative error Δ in the measurement of the upstream flow depth h_1 causes a relative error of 2.5 times Δ in the calculation of the flow rate Q. Thus, to minimize h_1 reading errors, a double-precision Vernier gauge was used during the experiment.

Experimental setup

The main intent of this section of the paper is to describe, as carefully as possible, the experimental setup used to test the various designed CWTFs.

Eight CWTFs of different contraction rates (Table 6) were made in Plexiglass. Each of them was used to measure the flow rate Q that passes through a trapezoidal-shaped approach channel. According to the notations adopted in Figs. 1 and 2, the approach channel was characterized by a base width $b_o = 0.25$ m, a height $h_o = 0.40$ m, and an angle of the sloped side from horizontal $\omega = 60°$, corresponding to a side slope $m_o = \cot(60°) = 0.57735$ horizontal to 1 vertical. Hence, the top with B_o of the approach channel was as follows:

$$B_o = b_o + 2 m_o h_o \tag{91}$$

That is,

$B_o = 0.71188$ m ≈ 0.712 m

According to Eq. (6), one may derive the following:

$$\theta_{\max} = 2\tan^{-1}\left(\frac{B_o}{2h_o}\right) = 2\times\tan^{-1}\left(\frac{0.71188}{2\times 0.40}\right) = 83.3285° \approx 83.33°$$

This is the apex angle value to not exceed for the triangular inlet section of the CWTFs involved in the planned experimental tests.

For the reasons mentioned during the section dedicated to the description of the device, the transition between each of the devices and the approach channel was ensured by an angle $\phi = 45°$, implying an angle $\gamma = 45/2 = 22.5°$ according to Eq. (26).

For each of the seven contraction rates adopted, the corresponding values of the ε parameter and those of the top width B of the inlet section of the device were calculated according to Eq. (3) and (2), respectively. Additionally, using Eqs. (5), (9) and (8), respectively, the apex angle θ of the inlet triangular section of the device, the top width b and the apex angle of the outlet section were determined for each device. The results of these calculations are grouped in Table 6.

Table 6: Characteristics of the eight considered devices

Device	$\beta = b/B$	ε Eq. (3)	B (m) Eq. (2)	θ (°) Eq. (5)	b (m) Eq. (9)	α (°) Eq. (8)
1	0.15	0.8727245	0.6213	75.66	0.0932	13.29
2	0.20	0.8793077	0.6260	76.08	0.1252	17.79
3	0.25	0.885991	0.6307	76.50	0.1577	22.30
4	0.30	0.8927766	0.6355	76.93	0.1906	26.81
5	0.35	0.899667	0.6404	77.36	0.2241	31.30
6	0.40	0.9066646	0.6454	77.79	0.2582	35.77
7	0.45	0.9137718	0.6505	78.23	0.2927	40.20
8	0.50	0.9209914	0.6556	78.67	0.3278	44.56

In the following, the sizing steps of the device characterized by the contraction rate $\beta =$ 0.15 are taken as an example. However, this approach has been submitted to all the devices considered in Table 6, resulting in the sizing of each of them. Thus, according to Eq. (13), the radius R_2 (Figs. 1, 3) is as follows:

$$R_2 = \frac{1}{4} B_o\ (1 - \varepsilon\ \beta\ ) = 0.25 \times 0.71188022 \times \left(1 - 0.8727245 \times 0.15\right) = 0.15467223\, m$$

That is,

$$R_2 \approx 15.5\, cm$$

For $\phi = 45°$, the x_D and y_D coordinates (Figs. 1, 3) are equal. They are defined by Eq. (16) as follows:

$$x_D = y_D = \frac{\sqrt{2}}{8}\ B_o\ (1 -\ \varepsilon\beta\ ) = \frac{\sqrt{2}}{8} \times 0.71188022 \times (1 -\ 0.8727245 \times 0.15\ ) = 0.10936978\ m$$

That is,

$$x_D = y_D \approx 10.93\ cm$$

According to Eq. (23), the vertical distance $\overline{\mathrm{PP'}}$ (Figs. 1, 3) is such that:

$$\overline{\mathrm{PP'}} = \frac{1}{4} B_o \left(1 - \frac{\sqrt{2}}{2}\right)(1 - \varepsilon\beta) = \frac{1}{4} \times 0.71188022 \times \left(1 - \frac{\sqrt{2}}{2}\right) \times (1 - 0.8727245 \times 0.15)$$

Hence,

$$\overline{\mathrm{PP'}} = 0.04530245\ \ m \approx 4.53\, cm$$

With the help of Fig. 3, one may then deduce the following:

$$\overline{DP}^{\,2} = x_D{}^2 + \overline{PP'}^{\,2}$$

That is,

$$\overline{DP} = \sqrt{0.10936978^2 + 0.04530245^2} = 0.118381\, m \approx 11.84\, cm$$

According to Eq. (29), the arc of circle PD $\cap$ is given as follows:

$$\mathrm{PD}\cap = \frac{1}{4} B_o (1 - \varepsilon\beta)\varphi = \frac{1}{4} \times 0.71188022 \times (1 - 0.8727245 \times 0.15) \times \frac{\pi}{4} = 0.12147928 m$$

That is,

$$\mathrm{PD}\cap \approx 12.15\,cm$$

According to Eq. (34) for $\phi = 45°$, the radius R_1 (Fig. 1, 3) is expressed as follows:

$$R_1 = \frac{1}{4}\left(3+2\sqrt{2}\right)B_o(1-\varepsilon\beta)$$
$$= \frac{1}{4}\times\left(3+2\sqrt{2}\right)\times 0.71188022\times(1-0.8727245\times 0.15)$$

Whence,

$$R_1 = 0.90149582\ \ m \approx 90.15\,cm$$

The length $\overline{\mathrm{ET}}$ (Figs. 1, 3) of the device's converging sections is given by Eq. (38), for $\phi = 45°$, as follows:

$$\overline{\mathrm{ET}} = \frac{1}{2}\left(\sqrt{3+2\sqrt{2}}-\frac{\sqrt{2}}{4}\right)B_o(1-\varepsilon\beta)$$
$$= 1.03033009\times 0.71188022\times(1-0.8727245\times 0.15)$$
$$= 0.63745381m \approx 63.75cm$$

Thanks to the previously calculated dimensions, the device characterized by the contraction rate $\beta = 0.15$ has been geometrically entirely defined and represented in Fig. (7). It was decided to provide this device with a throat length approximately equal to 70 cm, representing the length $\overline{\mathrm{VE}}$ (Fig. 7).

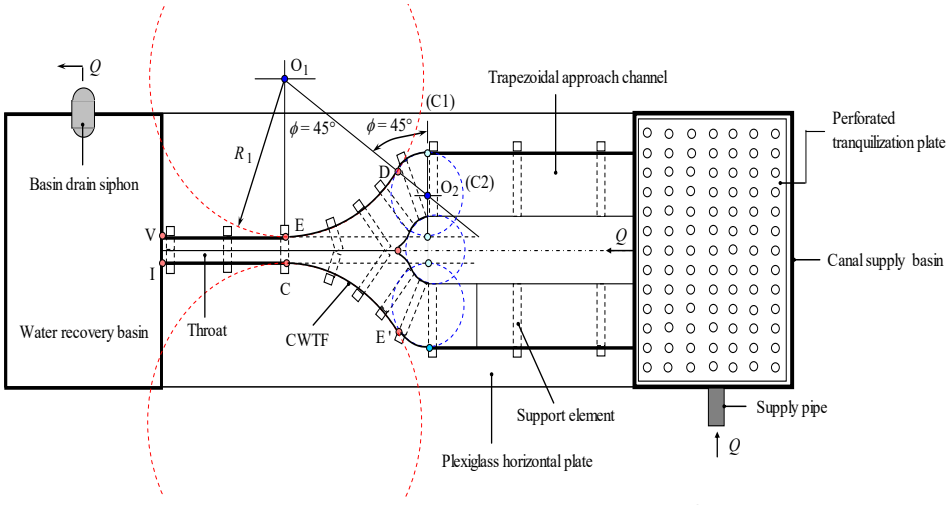

Figure 7: Plan view of the tested device of contraction rate $\beta = 0.15$ inserted in the experimental installation

Table 7 summarizes the main characteristics of the device characterized by a contraction rate $\beta = 0.15$, knowing that the top widths B and b are given in Table 6.

Table 7: Characteristics of the tested device characterized by a contraction rate $\beta =$ 0.15 and $\angle \phi = 45°$. Notations according to Figs. 1 and 3

β	R_1 (cm)	R_2 (cm)	$x_D = y_D$ (cm)	$\overline{PP'}$ (cm)	$\overline{ET}$ (cm)	$\overline{VE}$ (cm)
0.15	90.15	15.50	10.93	4.53	63.75	70

The walls of the device as well as those of the trapezoidal approach channel were made in one piece using a flexible Plexiglass plate 1 mm thick; its variable width was carefully calculated to ensure the same height h_o both for the approach channel and for the device, including the transition.

The installation represented in Fig. 7 was fed by an underground water storage tank working at a constant level and equipped with a submerged pump whose maximum flow rate was 60 l/s. The flow supplied by the pump was routed through a steel pipe over a certain distance in which a high-power and easy-to-use diaphragm flowmeter previously calibrated with care was inserted, which allowed the experimental flow rates to be measured at ± 0.2 l/s. At the outlet of the submerged pump, a valve is inserted into the steel pipe, making it possible to vary the flow rate and adjust it to the desired value. The rest of the pipe was made of flexible plastic, whose role was to convey the flow to the canal supply basin (Fig. 7). This was equipped with a perforated metal grid whose main role was to make the flow quiet at the inlet of the approach channel.

At the downstream outlet of the device, the flow is collected in a water recovery basin fitted with a siphon whose role is to drain the basin when the water has reached a certain level (Fig. 7). The water leaving the siphon is collected by a semiburied rectangular channel that carries the water to the underground water supply basin. Then, the flow repeats its itinerary, ensuring the closed-circuit operation of the aforementioned installation.

The measurement of the flow depth at the inlet section of the device must be as precise as possible because it significantly influences the flow rate. For this reason, the choice was made for the double precision Vernier gauge, which causes an absolute error of only 0.02 mm in the depth measurement.

During the tests, the flow rate Q was varied over the following wide range [0.545 l/s; 49 l/s], resulting in upstream depths h_1 varying in the range [6.35 cm; 38.95 cm]. The ranges of the upstream measured depth h_1 and the flow rate Q are summarized in Table 8 for each of the eight tested devices.

Table 8: Range of the flow rates Q and depths h_1 used for each of the eight tested devices

Device	Contraction rate β	Number of measurements	Discharge range (l/s)	Range of upstream depths (cm)
1	0.15	113	$0.63 \le Q \le 12.41$	$11.26 \le h_1 \le 37.05$
2	0.20	149	$0.72 \le Q \le 16.68$	$10.54 \le h_1 \le 37.05$
3	0.25	118	$0.628 \le Q \le 22.63$	$9.08 \le h_1 \le 38.06$
4	0.30	158	$0.704 \le Q \le 28.65$	$9.08 \le h_1 \le 38.69$
5	0.35	152	$0.545 \le Q \le 33.83$	$7.42 \le h_1 \le 38.64$
6	0.40	226	$0.572 \le Q \le 40.05$	$7.12 \le h_1 \le 38.95$
7	0.45	287	$0.578 \le Q \le 43.54$	$6.78 \le h_1 \le 38.12$
8	0.50	282	$0.557 \le Q \le 49.00$	$6.35 \le h_1 \le 38.02$

As shown in Table 8, each tested device is subjected to a series of flow rates Q delivered by the pump, which controls the admission of the flow. Each series of flow rates Q results in a series of upstream depths h_1. During the tests, the installation used allowed us to collect 1485 measurement points of the pair of parameters (Q, h_1), which corresponds to a representative sample on which reliable results and conclusions can be obtained.

RESULTS

This section is devoted to the experimental validation of Eq. (83), which governs the theoretical discharge coefficient $C_{d,Th}$. If this relationship is experimentally verified, then Eq. (86), which regulates the flow rate Q, should also be.

For each pair of experimentally measured values (Q_{Exp}, h_1), the experimental discharge coefficient $C_{d,Exp}$ is computed using the following relationship:

$$C_{d,Exp} = \frac{Q_{Exp}}{\sqrt{2g}\, m_2\, h_1^{5/2}} \tag{92}$$

Thus, the 1485 pairs (Q_{Exp}, h_1) collected during tests allowed us to calculate as many discharge coefficients $C_{d,Exp}$ with the help of Eq. (92).

Referring to Eq. (87) along with Eq. (86), $C_{d,Exp}$ should be constant for a given device under test, regardless of the pair of values (Q_{Exp}, h_1). Theoretically, the discharge coefficient calculated according to Eq. (92) would give a value that depends only on the contraction rate β of the tested device. For each of the tested devices, the calculation based on Eq. (92) shows that the obtained discharge coefficients vary around an average value, which is reported in Table 9. For each tested device, the deviation between the minimal and maximal experimental discharge coefficient values is extremely small. The maximum

deviation is approximately 0.891% obtained for $\beta = 0.30$. More precisely, the deviation varies between 0.77% and 0.891% in the considered range of β values. These deviations are probably due to handling errors during the tests. Additionally, no influence of the upstream depth h_1 on the discharge coefficient $C_{d,Exp}$ was observed, which means that Eq. (52), derived from dimensional analysis, reduces to the following:

$$C_d = \zeta(\beta) \tag{93}$$

Table 9 summarizes the values of the theoretical and average experimental discharge coefficients for each tested device, including the deviations between them.

Table 9: Experimental and theoretical values of the discharge coefficients for each tested device

Device	β	$C_{d,Exp}$ Eq. (85)		Average $C_{d,Exp}$	$C_{d,Th}$ Eq. (80)	Deviation (%)
		Min. Value	Max. Value			
1	0.15	0.28621568	0.28871441	0.2874825	0.28754976	0.0243
2	0.20	0.28742939	0.28981651	0.2885983	0.28860667	0.0029
3	0.25	0.28862706	0.29098787	0.2898326	0.2899924	0.0551
4	0.30	0.29030159	0.29291223	0.2916712	0.2917289	0.0198
5	0.35	0.29268030	0.29510011	0.2936831	0.29384524	0.0680
6	0.40	0.29497287	0.29756542	0.2962548	0.29637927	0.0420
7	0.45	0.29792914	0.30057013	0.2991708	0.2993802	0.070
8	0.50	0.30143525	0.30412473	0.3027775	0.30291208	0.0444

The maximum deviation between the average value of the experimental discharge coefficient $C_{d,Exp}$ and that of the theoretical discharge coefficient $C_{d,Th}$ is 0.07%. This means that Eq. (87), which governs the theoretical discharge coefficient, is experimentally verified. It can then be used with confidence in the range of validity $0.15 \leq \beta \leq 0.50$, without undergoing any correction.

Using Table 9, Fig. 8 shows the variation in the discharge coefficient C_d as a function of the contraction rate β. The discharge coefficient C_d increases with increasing contraction rate β, which was expected. The open signs, corresponding to the average values of the experimental discharge coefficient, are close to the theoretical predictions.

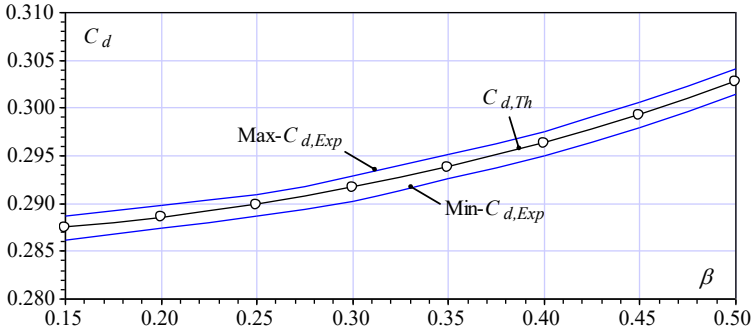

Figure 8: Variation in C_d (β) according to Table 9. (o) Average $C_{d,Exp}$ value

Additionally, in the range of validity $15 \leq \beta \leq 0.50$, the discharge coefficient of the device is in no way influenced by the upstream flow depth h_1. Outside this range, further testing is needed.

However, based on observations and graphical optimization calculations involving many configurations with $\phi = 45°$, the authors recommend adopting the ratio $B/B_o = \varepsilon = 0.918$ corresponding to a contraction rate $\beta = 0.48$, according to Eq. (3), for which the dimensions of the device are ideal. The perfect geometrical similarity of the triangle was the basis of this optimization study, which made it possible to write that the ratios B/h_o and b/h_o are constants for a given apex angle in accordance with Eqs. (4) and (7), respectively. Furthermore, the recommended value $\varepsilon = 0.918$ results in a transition between the approach channel and the device that is neither too short nor too long. Additionally, for the optimal contraction rate $\beta = 0.48$, the length $\overline{ET}$ of the converging sections of the device (Figs. 1 and 3) is such that $\overline{ET} / B_o \approx 0.5763$ according to Eq. (38).

For the best design of the throat, it is recommended to adopt the ratio "Throat Length"/B_o = $\overline{EV}/B_o$ = 0.60, according to the notations of Fig. 1.

Table 10 records the geometrical characteristics of the device recommended by the authors. The recommended characteristics are related to the top width B_o of the approach channel.

Table 10: Geometrical characteristics of the ideal CWTF corresponding to $\beta = 0.48$ and $\phi = 45°$. Notations according to Fig. 1

B/B_o	0.918
b/B_o	0.4407
R_2/B_o	0.140
R_1/B_o	0.815
$x_D/B_o = y_D/B_o$	0.0989
PD $\cap/B_o$	0.110
$\overline{\mathrm{ET}}/B_o$	0.5763
$\overline{\mathrm{VE}}/B_o$	0.600
$\ell(x)/B_o$Eq. (45)	$0.4407 + 1.63\left(1 - \sqrt{1 - 1.505(x/B_o)^2}\right)$

CONCLUSION

The paper addressed down to the tiniest detail a new type of flume. This is the curved wall triangular flume, abbreviated CWTF, composed of a converging triangular section whose opening angle is variable along its entire length. It is endowed with a throat downstream, which is likewise a triangular section, with a constant apex angle. Except for the difference in the cross-section shape, the CWTF has the configuration of the modified Parshall. It brings together the advantages of the V-notch and those of the Parshall. The triangular section provides better accuracy in measuring the flow rate, whether low or high, while the Parshall provides notably a single-valued function between the flow rate and upstream depth due to its design.

It has been shown that the converging section is generated by two circles tangent to each other and tangent to a horizontal straight line passing along the top edge of the throat [Fig. (1)]. To allow the designer to easily achieve the geometry of the device, the appropriate dimensions of the flume have been presented in the form of dimensionless ratios, relating them to the top width B_o of the approach channel regardless of its shape [Eqs. 1 to 45]. These have been carefully derived from indisputable geometrical considerations. It was observed that the dimensions of the device were only dependent on the contraction rate β of the converging section after setting the angle ϕ, which ensures a smooth transition between the flume and the approach channel; the contraction rate β was defined as the ratio of the top width b of the outlet section to the top width B of the inlet section of the device, i.e., $\beta = b/B$.

The study has been ongoing with the analytical determination of the stage-discharge relationship, hence that of the discharge coefficient of the device, after having theoretically hypothesized the formation of a control section somewhere inside the throat. The observations made in the laboratory on the behavior of the flow in the eight tested devices strengthened this hypothesis.

The stage-discharge relationship has been successfully determined following two different rigorous theoretical approaches while taking into account the effect of the approach flow velocity. The first method consisted of judiciously manipulating the energy equation applied between the inlet sections of the device and the throat. After some mathematical developments, implicit Eq. (68) in h_1^* has been obtained solely depending on the contraction rate β of the device. To avoid iterative calculations, Eq. (68) was approximated by the Hoerl model, which led to the approximate Eq. (69). The maximum deviation between the exact Eq. (68) and approximate Eq. (69) is less than 0.53% within the wide range $0.15 \leq \beta \leq 0.80$, inducing a maximum error less than 1.27% in the discharge coefficient C_d computation according to Eq. (73). If this error is not appropriate, the user can calculate the exact value of h_1^* by subjecting the implicit Eq. (68) to an iterative process whose speed of convergence will be improved by introducing the initial value $h_{1,0}^*$ computed according to Eq. (69). This allows the calculation of an exact theoretical value of the discharge coefficient C_d according to Eq. (72).

The second method adopted consisted of expressing the kinetic factor δ, which is closely related to the approach flow velocity, as expressed by Eq. (74). The upstream velocity head is correctly assumed to be a fraction of the corresponding upstream flow depth h_1. After appropriate manipulations, the kinetic factor δ was expressed as a function of the contraction rate β of the device in accordance with Eq. (81). Due to its implicit character, Eq. (81) has been expanded in a Taylor series up to the second-order, resulting in the quadratic Eq. (84), whose real solution is given by the explicit Eq. (85). This allowed us to deduce Eq. (87), which governs the theoretical discharge coefficient C_d. Eq. (87) along with Eq. (86) is a very accurate theoretical formula that can be used with great confidence.

The study was pursued by a deep experimental protocol conducted on eight devices characterized by a contraction rate β varying in the range [0.15; 0.50]. The devices were tested in an appropriate installation that allowed us to collect nearly 1500 measurement points of the pair of parameters (discharge Q; upstream flow depth h_1). The main objective of the tests was to validate or refine the theoretical discharge coefficient C_d relationship in accordance with the obtained experimental results. For all the tested devices, the analysis of the experimental measurements revealed excellent agreement between the theoretical and experimental discharge coefficients. The calculated maximum deviation was only 0.07%, which means that Eq. (87), which governs the theoretical discharge coefficient C_d of the device, does not need any correction, provided respecting the following range of validity $0.15 \leq \beta \leq 0.50$.

By the end of the paper, using an optimization procedure, the authors recommended the use of an ideal CWTF characterized by a contraction rate $\beta = 0.48$. The dimensions of the device, related to the top width B_o of the approach channel, are presented.

The future planned research concerns the second version of the device equipped with a downstream diverging section or discharge. It serves to ensure the connection between the throat and the downstream walls of the main channel and to be the seat of a hydraulic jump. The main role of the hydraulic jump is to transform the strong kinetic energy in the

throat into potential energy in the converging section, allowing the device to operate with a minimum of head losses. It is then required to determine the limit of the semimodularity beyond which the flow rate is no longer a single-valued function of the upstream depth h_1. The limit of the semimodularity, which corresponds to the ratio of the total downstream head to the total upstream head, will define the head losses caused by the device; these losses should be as low as possible, representing only a few percent of the total head, which is likewise approximately equivalent to the head loss required for proper operation of a similar suppressed weir for which the potential energy accumulated upstream is almost entirely lost downstream.

Declaration of competing interest

The authors declare that they have no known competing financial interests or personal relationships that could have appeared to influence the work reported in this paper.

REFERENCES

ACHOUR B. (1984). Design and production of a dihedral flowmeter with hydraulic jump with or without sill, Magister Thesis, National Polytechnic School of Algiers. (In French)

ACHOUR B., AMARA L. (2022). Flow measurement using a triangular broad-crested weir, theory and experimental validation, Flow Measurement and Instrumentation, Vol. 83, Paper 102088.

ACHOUR B., BOUZIANE M.T., NEBBAR M.L. (2003) Triangular broad-crested flowmeter in a rectangular channel, Larhyss Journal, No 2, pp. 7–43. (In French)

ACKERS P., HARRISON A.J.M. (1963). Critical depth flumes for slow measurement in open channels, Hydraulics research paper No. 5, Hydraulics Research Station, Wallingford, Berkshire, England.

ANIRUDDHA D.G, ANKUR K., AVINASH B.M. (2020). Cylindrical Central Baffle Flume for Flow Measurements in Open Channels, Technical Note, Journal of Irrigation and Drainage Engineering, Vol. 146, Issue 9, pp. 1-9.

ASTM D5390 – 93. (2013). Standard Test Method for Open-Channel Flow Measurement of Water with Palmer-Bowlus Flumes.

BIJANKHAN M., FERRO V. (2019). Experimental study on triangular central baffle flume, Flow Measurement and Instrumentation, Vol. 70, Paper 101641.

BOS M.G. (1976). Discharge Measurement Structures, Laboratorium Voor Hydraulica Aan Afvoerhydrologie, Landbouwhogeschool, Wageningen, The Netherlands.

BOS M.G. (1989)., Discharge Measurement Structures, third ed., Publication 20, Int. Institute for Land Reclamation and Improvement, Wageningen, The Netherlands.

CARLIER M. (1998). General and applied hydraulics, Collection of the Department of Studies and Research of Electricité de France, Ed. Eyrolles, Paris, France.

CHOW V.T. (1959) Open Channel Hydraulics. McGraw-Hill, New York.

CLEMMENS A., BOS M.G., REPLOGLE J. (1984). Portable RBC Flumes for Furrows and Earthen Channels, Transactions ASAE, Vol. 27, Issue 4.

FERRO V. (2016). Simple flume with a central baffle, Flow Measurement and Instrumentation, Vol. 52, pp. 53–56.

GWINN W.R., PARSONS D.A. (1976). Discharge Equations for HS, H, and HL Flumes, Journal of Hydraulic Division, Vol. 102, Issue 1.

HENDERSON F.M. (1966). Open Channel Flow, the McMillan Company, New York, N.Y, USA.

JOHNSON A. (1963). Modified Parshall Flume, U.S. Geological Survey.

KILPATRICK F., SCHNEIDER V. (1983). Use of Flumes in Measuring Discharge, U.S. Geological Survey, Techniques of Water-Resources Investigations, Book 3, Chapter A14.

KOLAVANI F.L., BIJANKHAN M., STEFANO C., DI FERRO V., MAZDEH A.M. (2019). Experimental study of central baffle flume, Journal of Irrigation and Drainage Engineering, Vol. 145, Issue 3.

KOLB W.M. (1983). Curve Fitting for Programmable Calculators, Imtec Publishing, Bowi, Maryland, USA.

LANGHAAR H.L. (1962). Dimensional Analysis and Theory of Models, Wiley and Sons Inc.

PARSHALL R.L. (1936). The improved Venturi flumes, Transactions ASCE, Vol. 89, pp. 841–880.

PERUGINELLI A., BONACCI F. (1997). Mobile prisms for flow measurement in rectangular channels, Journal of Irrigation and Drainage Engineering, Vol. 123, Issue 3, pp. 170–174.

ROBINSON A.R. (1966). Water Measurement in Small Irrigation Channel Using Trapezoidal Flumes, Transaction ASCE, Vol. 9, Issue 3, Paper 0382–0385.

ROBINSON A.R., CHAMBERLAIN A.R. (1960). Trapezoidal flumes for open-channel flow measurement, Transactions ASAE, Vol. 3, Issue 2, pp. 120-124.

SAMANI Z. (2017). Three simple flumes for flow measurement in open channels, Journal of Irrigation and Drainage Engineering, Vol. 143, Issue 6, Paper 04017010.

SAMANI Z., JORAT S., YOUSEF M. (1991). Hydraulic characteristics of circular flume, Journal of Irrigation and Drainage Engineering. ASCE, Vol. 117, Issue 4, pp. 558–566.

SAMANI Z., MAGALLANEZ H. (2000). Simple Flume for Flow Measurement in Open Channel, Journal of Irrgation and Drainage Engineering, ASCE, Vol. 126, Issue 2, pp. 127- 129.

SKOGERBOE G.V., BENNETT R.S., WALKER W.R. (1972). Generalized discharge relations for cutthroat flumes, Journal of Irrigation and Drainage Engineering, ASCE, Vol. 98, Issue 4, pp. 569–583

UNITED STATES DEPARTMENT OF THE INTERIOR, Bureau of Reclamation (2001). A guide to effective water measurement practices for better water management, A water resources technical publication, Water measurement manual, USA.

VATANKHAH A.R., KHAMISABADI M. (2019). General stage-discharge relationship for sharp-crested power law weirs: analytical and experimental study, Irrigation and Drainage, Vol. 68, Issue 4, pp. 808-821.